Electronic Supplementary Material (ESI) for Chemical Communications.
This journal is © The Royal Society of Chemistry 2019

Electronic Supplementary Information

Fe ions modulated formation of hollow NiFe oxyphosphide spheres with enhanced oxygen evolution performance

Yu Jia,[a†] Wei Cai,[ab†] Xiaoyu Li, [a] Xin-Yao Yu*[ab] and Zhanglian Hong*[a]

[a]School of Materials Science and Engineering, Zhejiang University, Hangzhou 310027, P. R. China. Email: hong_zhanglian@zju.edu.cn

[b]Institutes of Physical Science and Information Technology, Anhui University, Hefei 230601, P. R. China. E-mail: yuxinyao@ahu.edu.cn

[†]*These two authors contribute equally to this work.*

Experimental Section

Synthesis of yolk-shelled Ni-glycerate spheres: The yolk-shelled Ni glycerate spheres were synthesized according to the reference.[1] In a typical synthesis, 7.5 mL of glycerol was dissolved in 52.5 mL of isopropanol (IPA) under magnetic stirring for 10 min in a 100 mL Teflon container. Then, 145 mg of $Ni(NO_3)_2 \cdot 6H_2O$ was dissolved in the mixed solution under continuous magnetic stirring. When solution turned clear, 1 mL of H_2O was added into the above solution. After stirring for another 10 min, the container was transferred into a stainless autoclave and put in an electric oven at 200 °C for 12 h. After cooling down to the ambient temperature, the precipitates were collected by centrifugation and washed by ethanol for more than 3 times.

Synthesis of hollow Ni-glycerate spheres: In a typical synthesis, 15 mg of as-prepared yolk-shelled Ni-glycerate spheres were dispersed in 4 mL of ethanol to form solution A. 15 mg of $Fe(NO_3)_3 \cdot 9H_2O$ was dissolved in 6 mL of H_2O to form solution B. Then solution B was slowly added into solution A under continuously stirring. After stirring for 2 h, the precipitates were collected by centrifugation and washed by ethanol for more than 3 times.

Synthesis of hollow NiFe mixed metal glycerate spheres: In a typical synthesis, 5 mg of as-prepared hollow Ni-glycerate spheres were dispersed in 4 mL of ethanol to form solution A. 30 mg of $FeSO_4 \cdot 7H_2O$ was dissolved in 6 mL of H_2O to form solution B. Then solution B was slowly added into solution A under continuously stirring. After stirring for 2 h, the precipitates were collected by centrifugation and washed by ethanol for more than 3 times. For other Ni/Fe ratio samples, the procedure is similar expect for using 15 mg of $FeSO_4 \cdot 7H_2O$ and 45 mg of $FeSO_4 \cdot 7H_2O$ for solution B, respectively.

Synthesis of yolk-shelled NiFe mixed metal glycerate spheres: The procedure is similar to that for preparing hollow NiFe mixed metal glycerate spheres, expect for using yolk-shelled Ni-glycerate spheres for solution A.

Synthesis of hollow NiFe mixed metal oxyphosphide spheres: In a typical synthesis, 20 mg of as-obtained hollow NiFe mixed metal glycerate spheres and 200 mg of NaH_2PO_2 were put at two ends in a porcelain boat with NaH_2PO_2 locating on the upstream side of the tube furnace. Then, the samples were annealed at 300 °C for 2 h

with a ramping rate of 1°C min^{-1} under a flow of argon gas.

Synthesis of yolk-shelled NiFe mixed metal oxyphosphide spheres: The procedure is similar to that for preparing hollow NiFe mixed metal oxyphosphide spheres, expect for using yolk-shelled NiFe mixed metal glycerate spheres for phosphorization.

Synthesis of hollow Ni oxyphosphide spheres: The procedure is similar to that for preparing hollow NiFe mixed metal oxyphosphide spheres, expect for using hollow Ni-glycerate spheres for phosphorization.

Synthesis of yolk-shelled Ni oxyphosphide spheres: The procedure is similar to that for preparing hollow NiFe mixed metal oxyphosphide spheres, expect for using yolk-shelled Ni-glycerate spheres for phosphorization.

Synthesis of NiFe-LDH: In a typical synthesis, 300 mg of urea was dissolved in 35 mL of H_2O under constant magnetic stirring in a 100 mL Teflon container. Then 696 mg of $Ni(NO_3)_2 \cdot 6H_2O$ and 323 mg of $Fe(NO_3)_3 \cdot 9H_2O$ were added in and dissolved in the solution. After stirring for another 10 min, the container was transferred into a stainless autoclave and put in an electric oven at 120 °C for 12 h. After cooling down to the ambient temperature, the precipitates were collected by centrifugation and washed by ethanol for more than 3 times.

Material Characterizations

The XRD patterns were collected on X'Pert PRO, PANnalytical (Cu Kα radiation, λ = 1.540598 Å). The morphology and structure of products were characterized using FESEM (Phenom) equipped with EDX, and TEM (JEM-1200EX). The HRTEM images, HAADF-STEM images and elemental images were collected using TEM (Jeol 2100F) equipped with EDX. XPS were carried out on Thermo Scientific K-Alpha+. Raman spectra were collected on an Edinburgh RM5 Raman microscope equipped with a 514 nm excitation laser.

Electrochemical Measurements

For OER tests, all tests were performed in 1 M KOH. The electrochemical measurements were performed with a CHI 760E electrochemistry workstation (CHI

instruments, Inc., Shanghai) using three-electrode system. Rotating disk electrode (RDE) was used as that working electrode that rotate at 1600 rpm to get rid of generated oxygen bubbles. Hg/HgO electrode and graphite rod was used as reference electrode and counter electrode, respectively. To prepare working electrode, 5.0 mg of catalysts were dispersed in 270 μL of ethanol, 200 μL of H_2O, and 30 μL of 5 wt% Nafion solution for 30 min to form a heterogeneous ink. Then 5 μL of the catalyst ink was dropped onto a polished glassy carbon rotating disk electrode with a diameter of 5 mm (0.25 mg cm^{-2}). Then, the electrode was dried at ambient temperature. Linear sweep voltammetry was performed at a scan rate of 5 mV s^{-1} for polarization curves. Polarization curves were corrected for *iR*-compensation. Electrochemical impedance spectroscopy (EIS) of the electrodes were measured in the frequency range from 10^5 to 0.1 Hz with 5 mV amplitude. The electrochemically capacitance surface area (ECSA) was estimated from the electrochemical double-layer capacitance (C_{dl}, EDLC). The EDLC measurements were carried out by conducting a series of cyclic voltammetry (CV) between 1.14 V and 1.24 V versus RHE at different scan rates. The difference of current densities at 1.19 V versus RHE from different scan rates were plotted with those scan rates. The slope of this fitted line equals to half of C_{dl}. For stability tests, working electrodes were prepared by dropping 50 μL of the above-mentioned catalyst ink onto carbon fiber paper with an active surface area of 0.5 cm^2. The catalysts were conducted a chronoamperometric test for 20 hours at a static overpotential of 270 mV.

For ORR tests, 0.1 M KOH is used as electrolyte. The configuration is similar to OER tests. Rotating ring-disk electrode (RRDE) with a Pt ring (4 mm diameter for disk electrode, 5 mm inner diameter and 7 mm outer diameter for Pt ring) is used as the working electrode. Saturated Calomel Electrode (SCE) is used as reference electrode. Before the test, N_2/O_2 was purged into the 0.1 M KOH for 30 min to achieve N_2/O_2 saturated solution. CV curves were then obtained at a scan rate of 100 mV s^{-1}. LSV curves were obtained at a scan rate of 5 mV s^{-1} in the potential range from 1.0 V to 0.2 V (*vs*. RHE). EDLC measurements were conducted by a series of CV tests in the potential range from 0.81 V to 1.01 V (*vs*. RHE).

The H_2O_2 selectivity ($HO_2^-\%$) and electrons transferred number (n) are calculated by the following formulas:

$$n = \frac{4 \times i_d}{i_d + \frac{i_r}{N}}$$

$$HO_2^-\% = \frac{200 \times \frac{i_r}{N}}{i_d + \frac{i_r}{N}}$$

Here i_d is the disk current, i_r is the ring current and N is the current collection efficiency of the Pt ring in RRDE electrode (0.424 for this electrode).

TOF calculation

TOF values were calculated according to the following formula:[2]

$$TOF = \frac{I}{4 \times F \times m}$$

I (ampere) refers to the current at a certain overpotential. *4* refers to the number of electrons transferred in 1 mol oxygen evolution. F refers to Faraday constant (96485 C mol^{-1}) and m is the number of moles of active species.

To estimate m, we conduct a series of CV tests at different scan rates. A linear plot of oxidation currents and scan rates can be obtained from CV curves. After fitting the slope of the linear plot, the quantity of m is calculated according to the formula:

$$Slope = \frac{n^2F^2m}{4RT}$$

In this formula, n is the number of transferred electrons (here n=1). F is Faraday constant, m is the number of moles of active species. R and T are ideal gas constant (8.314 J mol^{-1} K^{-1}) and absolute temperature (298 K), respectively.

Therefore, TOF values can be obtained based on m and current at a certain overpotential.

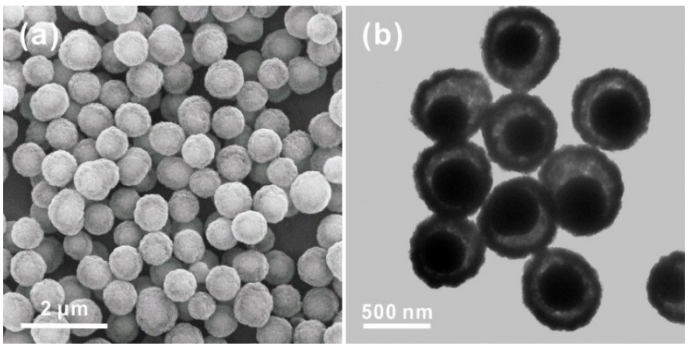

Fig. S1 (a) FESEM and (b) TEM image of YS-Ni-gly spheres.

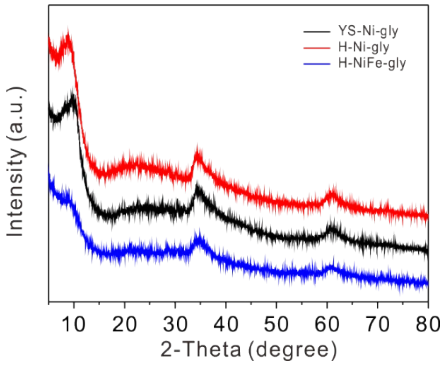

Fig. S2 XRD patterns of YS-Ni-gly, H-Ni-gly, and H-NiFe-gly spheres.

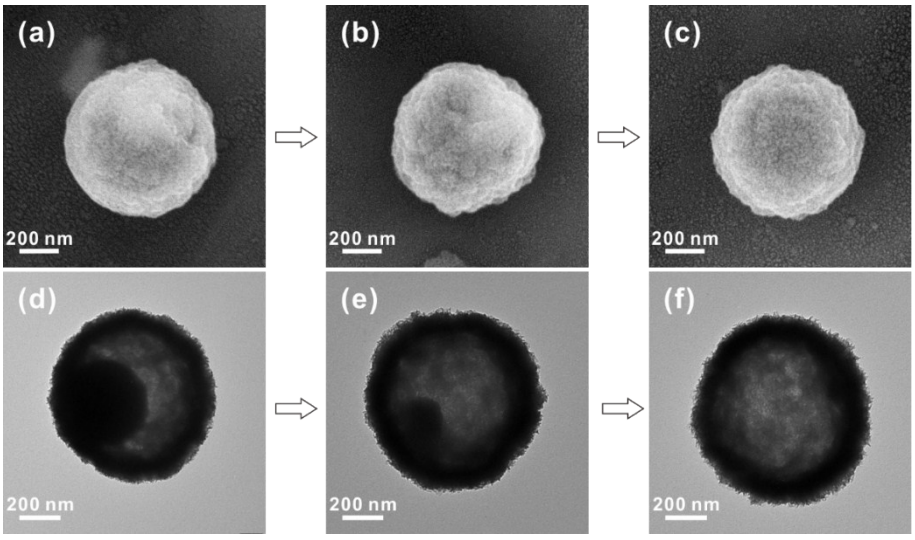

Fig. S3 Hollowing process of YS-Ni-gly: (a-c) FESEM images and (d-f) TEM images obtained from different reaction time of YS-Ni-gly sphere reacting with Fe^{3+} for (a,d) 30 min, (b,e) 1 h, and (c,f) 2 h.

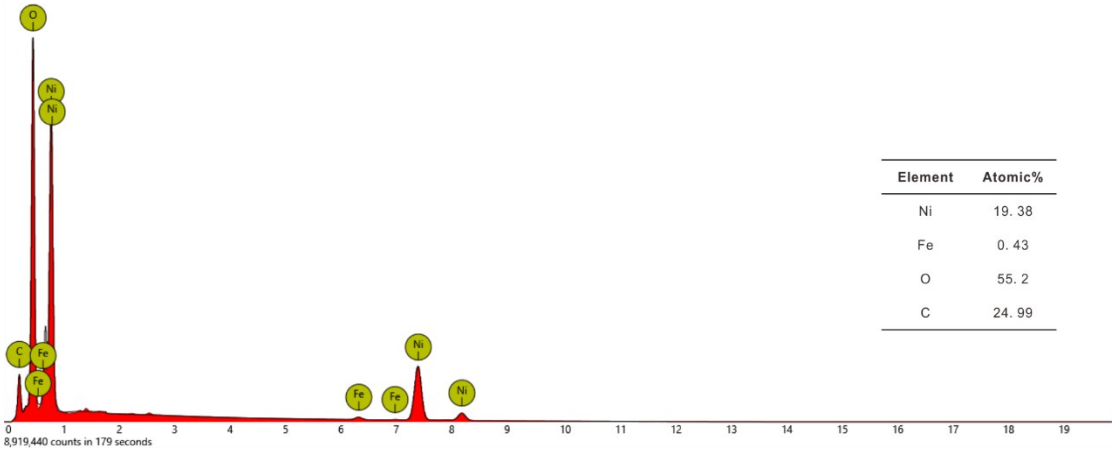

Fig. S4 EDX spectrum of the YS-Ni-gly spheres after reacting with Fe^{3+} for 2 h.

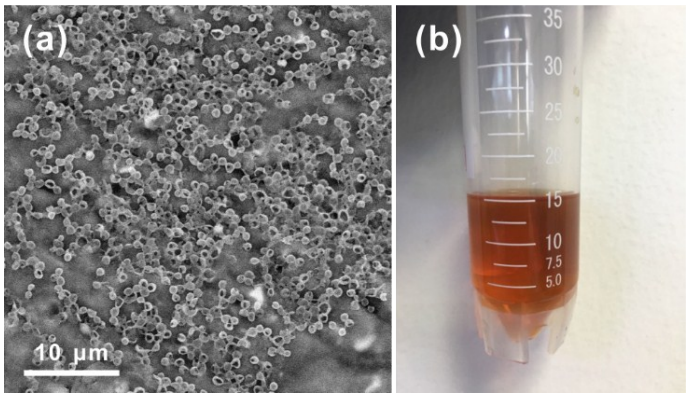

Fig. S5 (a) FESEM image of the YS-Ni-gly spheres after reacting with Fe^{3+} for 4 h; (b) digital image of solution indicating that YS-Ni-gly spheres completely dissolve after reacting with Fe^{3+} for 12 h.

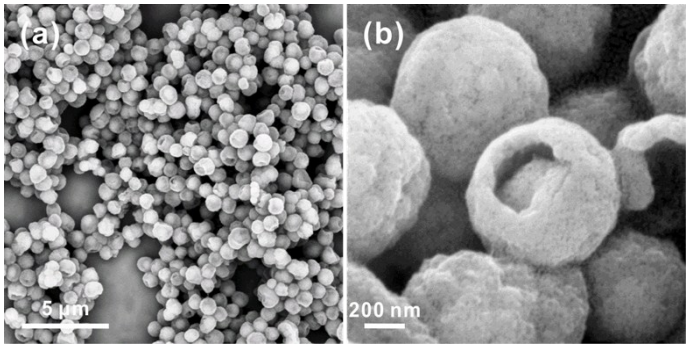

Fig. S6 (a,b) FESEM images of the YS-Ni-gly spheres after reacting with the HCl solution that has the same pH of $Fe(NO_3)_3$ solution for 2 h.

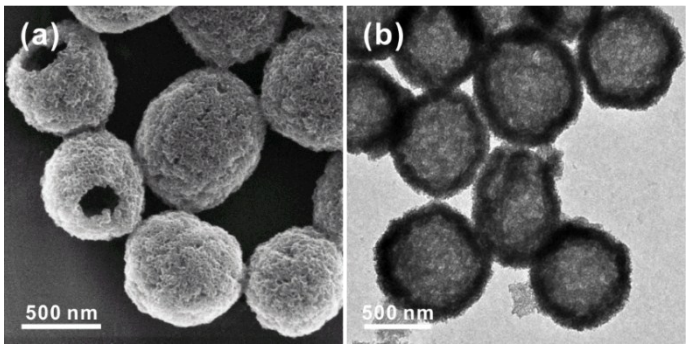

Fig. S7 (a) FESEM image and (b) TEM image of the YS-Ni-gly spheres after reacting with the $FeCl_3$ solution for 2 h. Therefore, a possible redox reaction happens first between the core of YS-Ni-gly and Fe^{3+} and the core gradually dissolves. After the core is completely etched out, the shell of YS-Ni-gly begins to react with Fe^{3+} and dissolves at last. The preferential etching of the core at first may result from the different thermodynamic characters of the core and the shell in YS-Ni-gly spheres.

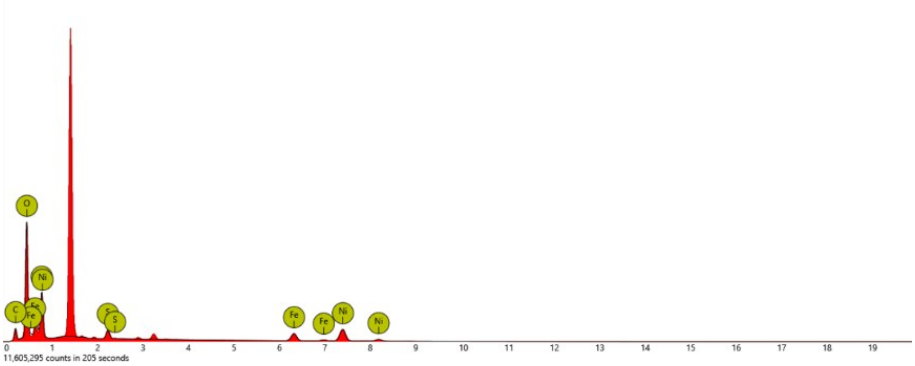

Fig. S8 EDX spectrum of H-NiFe-gly spheres (the sharp peak at between 1-2 keV is attributed to Al substrate; S element may come from $FeSO_4$).

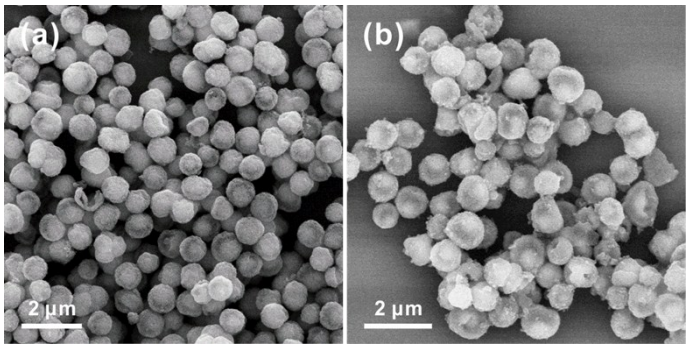

Fig. S9 FESEM images of (a) YS-Ni-gly spheres after reacting with Fe^{2+} for 2 h and (b) YS-Ni-gly spheres after reacting with Fe^{2+} for 12 h.

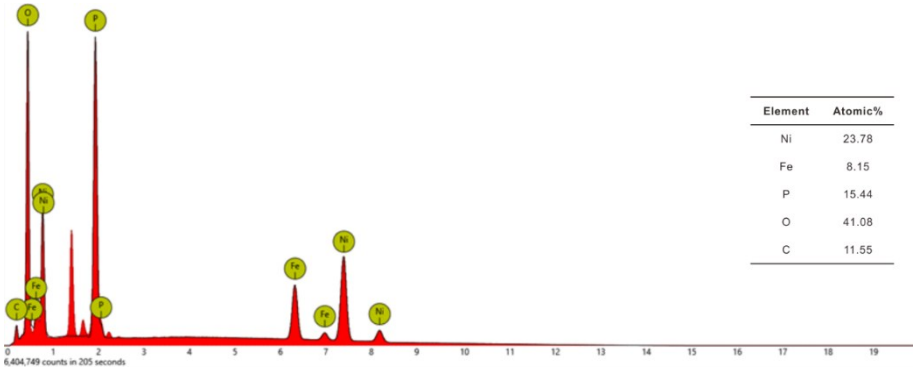

Fig. S10 EDX spectrum of H-NiFe oxyphosphide spheres.

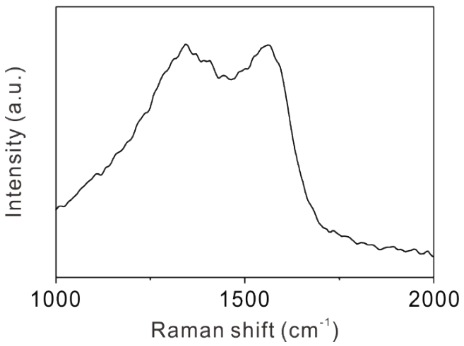

Fig. S11 Raman spectrum of H-NiFe oxyphosphide spheres.

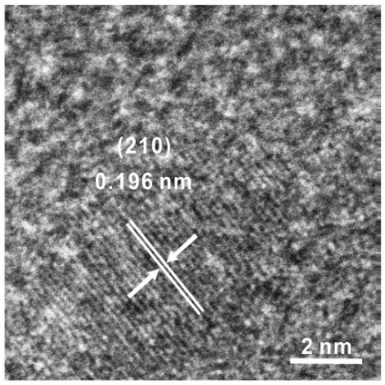

Fig. S12 HRTEM image of H-NiFe oxyphosphide spheres.

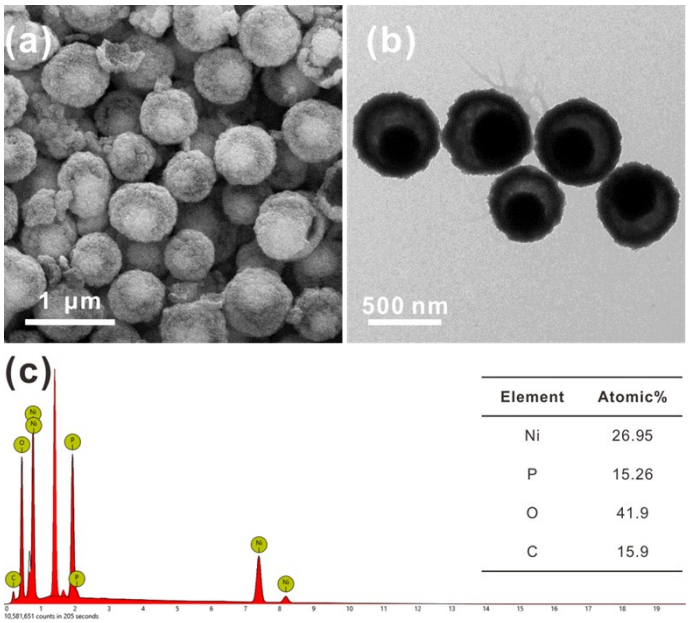

Fig. S13 (a) FESEM image, (b) TEM image, and (c) EDX spectrum of YS-Ni oxyphosphide spheres.

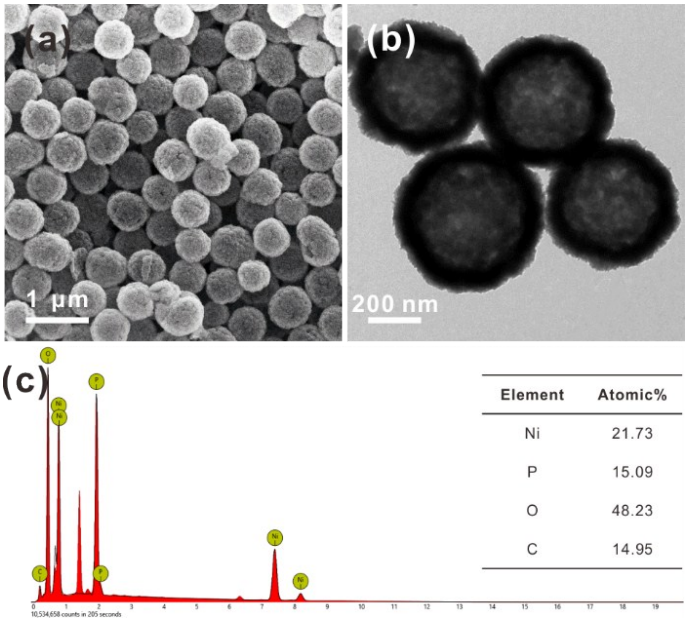

Fig. S14 (a) FESEM image, (b) TEM image, and (c) EDX spectrum of H-Ni oxyphosphide spheres.

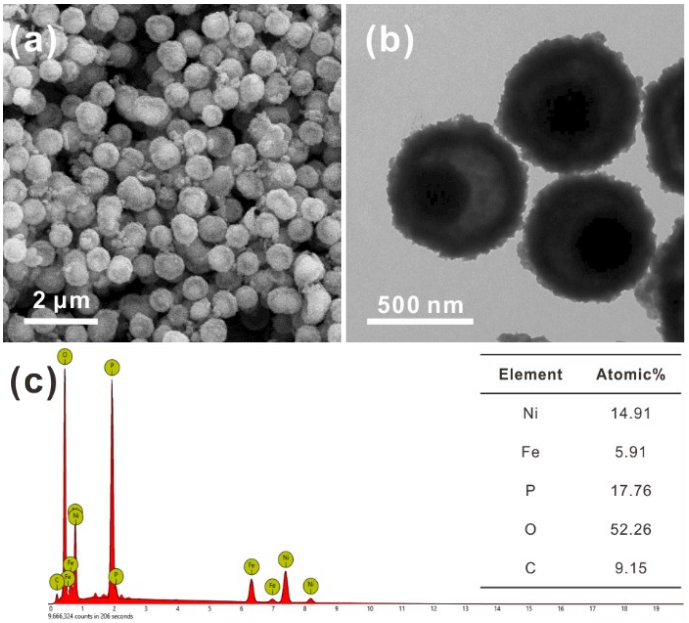

Fig. S15 (a) FESEM image, (b) TEM image, and (c) EDX spectrum of YS-NiFe oxyphosphide spheres.

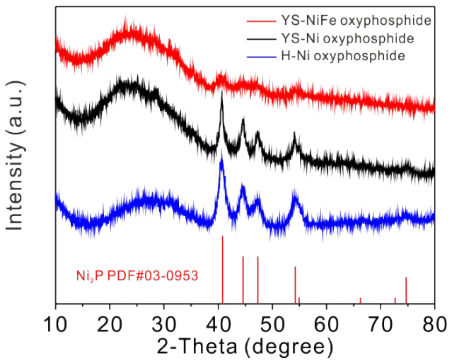

Fig. S16 XRD patterns of YS-NiFe oxyphosphide spheres, YS-Ni oxyphosphide spheres, and H-Ni oxyphosphide spheres.

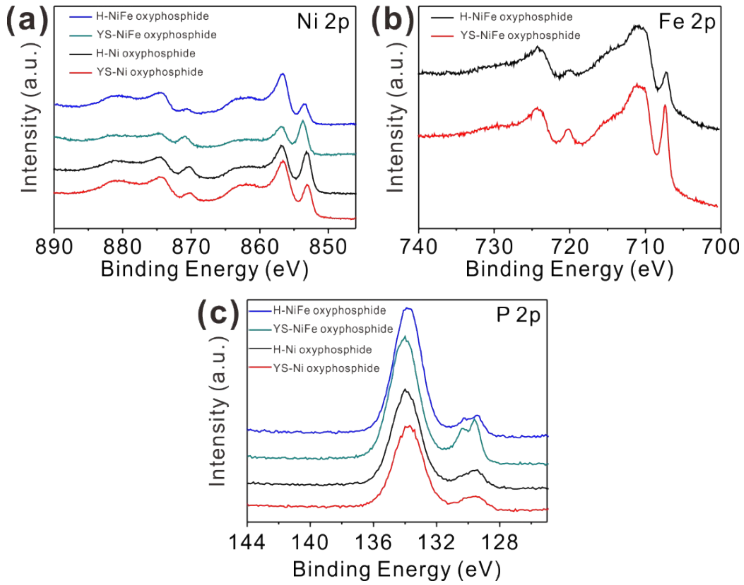

Fig. S17 (a) Ni 2p, (b) Fe 2p and (c) P 2p XPS spectra of H-NiFe, YS-NiFe, H-Ni, and YS-Ni oxyphosphide spheres.

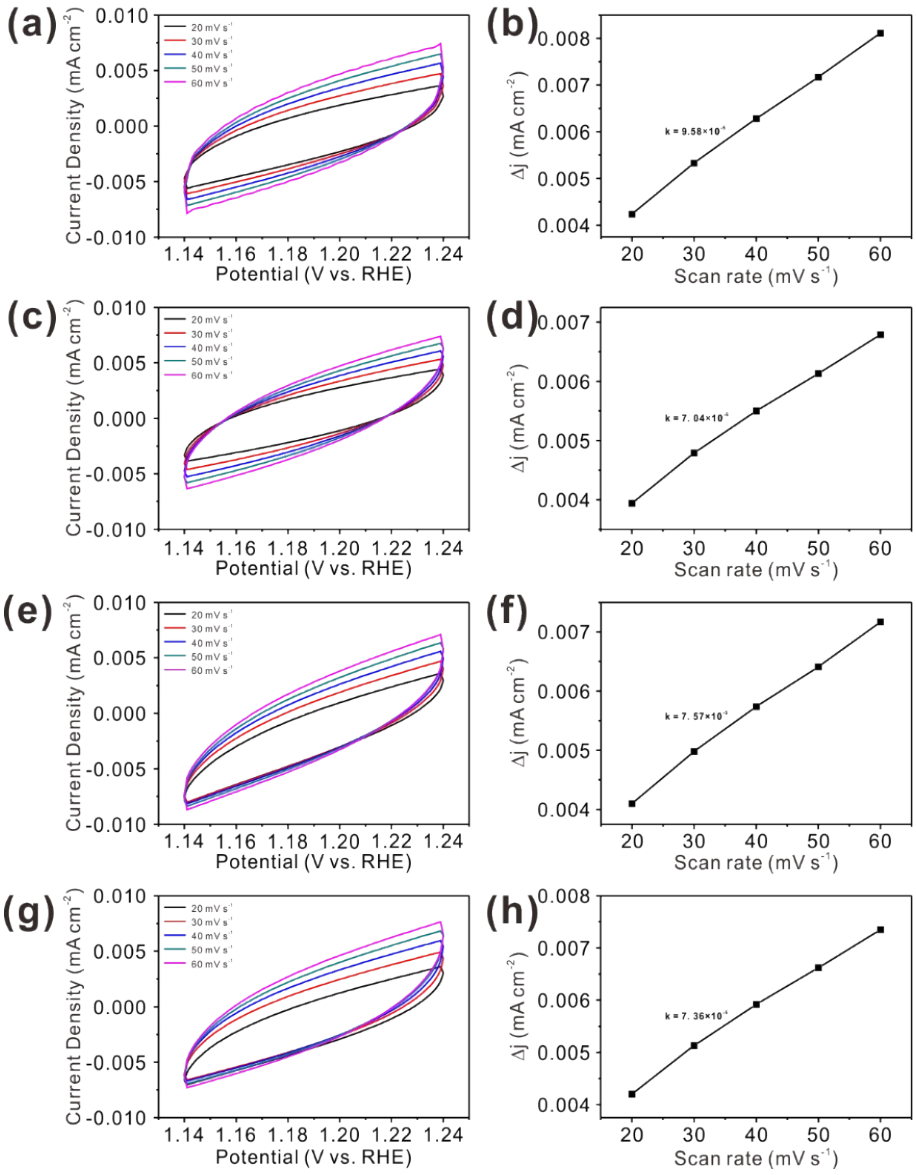

Fig. S18 CV curves of (a) H-NiFe, (c) YS-NiFe, (e) H-Ni, and (g) YS-Ni oxyphosphide spheres at scan rates of 20, 30, 40, 50, and 60 mV s^{-1}. (b), (d), (f) and (h) current density difference (Δj) at 1.19 V plotted as a function of different scan rates derived from (a), (c), (e) and (g), respectively. The value of C_{dl} equals to half of the slope of the fitted line.

For H-NiFe oxyphosphide, $C_{dl} = 0.5 \times 9.58 \times 10^{-5} \times 10^{6}$ μF $cm^{-2} = 47.9$ μF cm^{-2}

For YS-NiFe oxyphosphide, $C_{dl} = 0.5 \times 7.04 \times 10^{-5} \times 10^{6}$ μF $cm^{-2} = 35.2$ μF cm^{-2}

For H-Ni oxyphosphide, $C_{dl} = 0.5 \times 7.57 \times 10^{-5} \times 10^{6}$ μF $cm^{-2} = 37.9$ μF cm^{-2}

For YS-Ni oxyphosphide, $C_{dl} = 0.5 \times 7.36 \times 10^{-5} \times 10^{6}$ μF $cm^{-2} = 36.8$ μF cm^{-2}

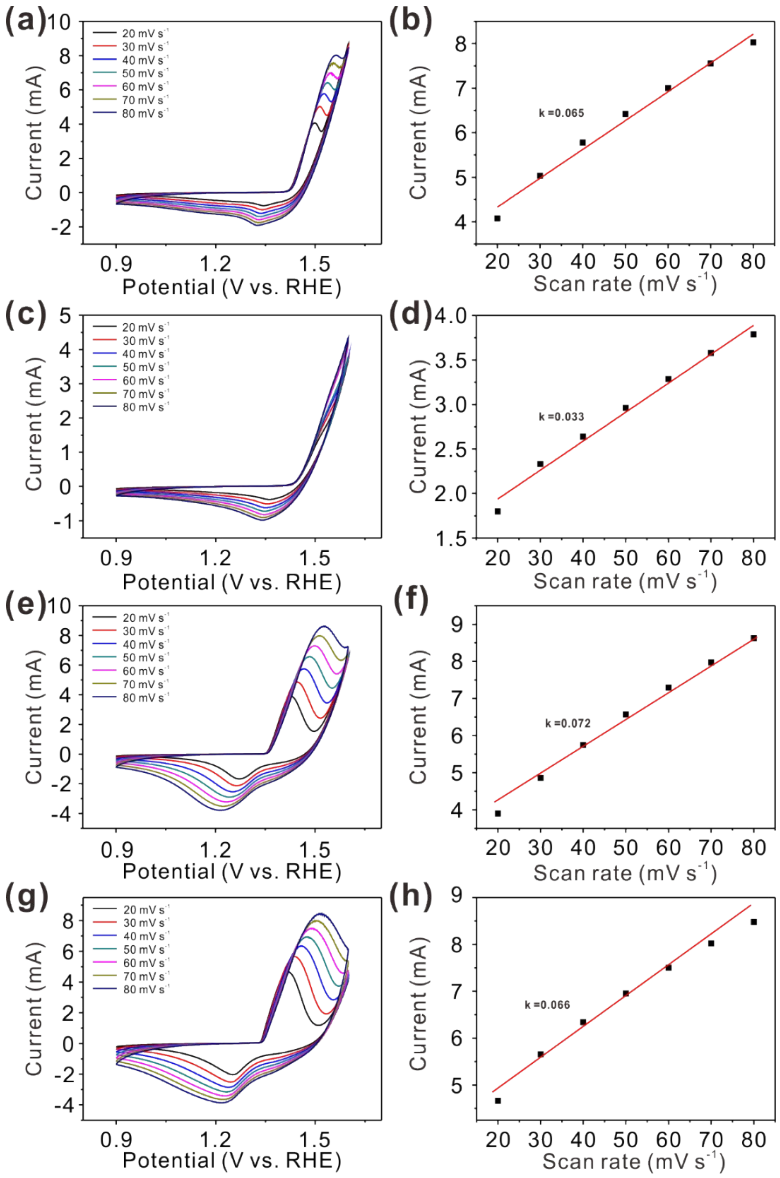

Fig. S19 CV curves of (a) H-NiFe, (c) YS-NiFe, (e) H-Ni, and (g) YS-Ni oxyphosphide spheres at scan rates of 20~80 mV s^{-1}, (b), (d), (f) and (h) Linear relationship of the oxidation peak current and scan rates for the corresponding samples.

Based on the formula, Slope = $\frac{n^2F^2m}{4RT}$, m (the number of moles of active species) can be calculated.

$m_{\text{H - NiFe oxyphosphide}} = 6.92 \times 10^{-8}$ mol, $m_{YS\text{ - NiFe oxyphosphide}} = 3.51 \times 10^{-8}$ mol

$m_{\text{H - Ni oxyphosphide}} = 7.66 \times 10^{-8}$ mol, $m_{YS\text{ - Ni oxyphosphide}} = 7.03 \times 10^{-8}$ mol

Then TOF values are calculated based on the formula $\mathrm{TOF} = \frac{I}{4 \times F \times m}$.

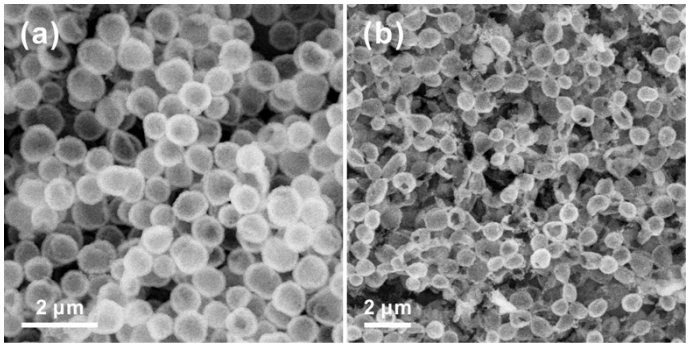

Fig. S20 FESEM images of the products of H-Ni-gly spheres after reacting with different concentration of $FeSO_4 \cdot 7H_2O$: (a) 2.5 mg mL^{-1} and (b) 7.5 mg mL^{-1}.

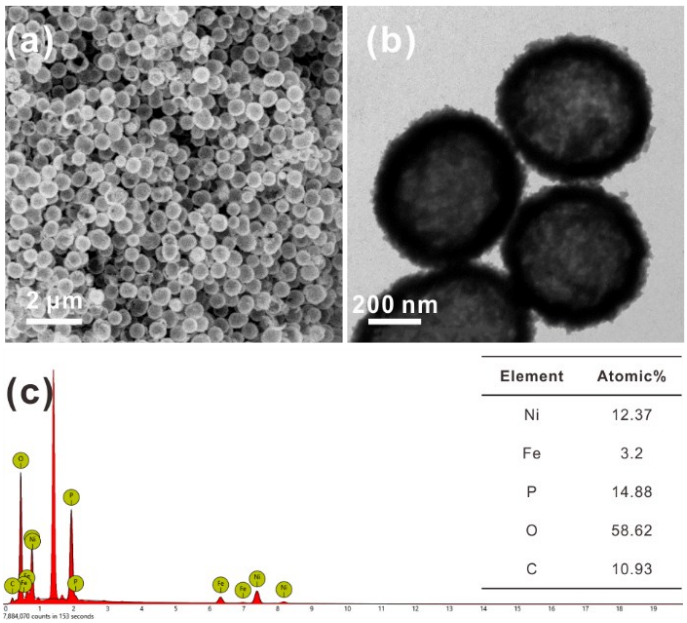

Fig. S21 (a) FESEM image, (b) TEM image, and (c) EDX spectrum of NFOP-1.

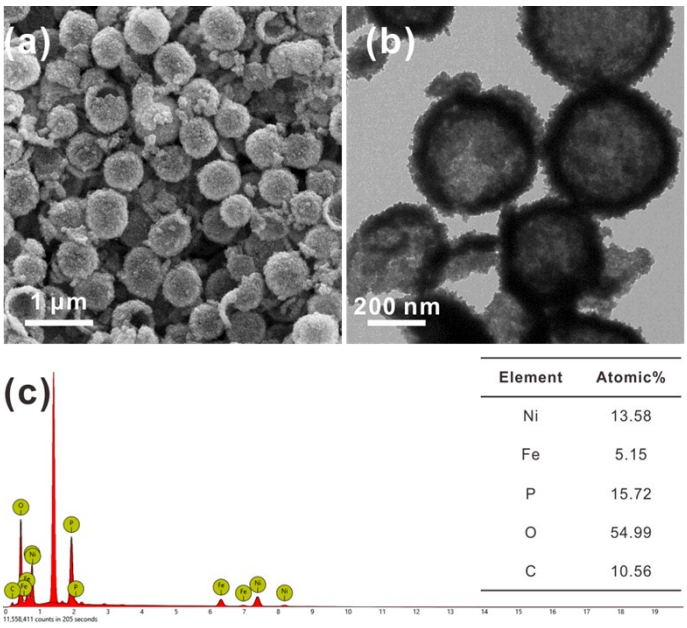

Fig. S22 (a) FESEM image, (b) TEM image, and (c) EDX spectrum of NFOP-2. The change in the Ni/Fe atomic ratio in NFOP-2 is not proportional to the concentration of Fe^{2+}, indicating that the incorporated concentration of Fe using the current ion-exchange method may reach saturation. However, a larger concentration of Fe^{2+} will lead to the collapse of the hollow structure.

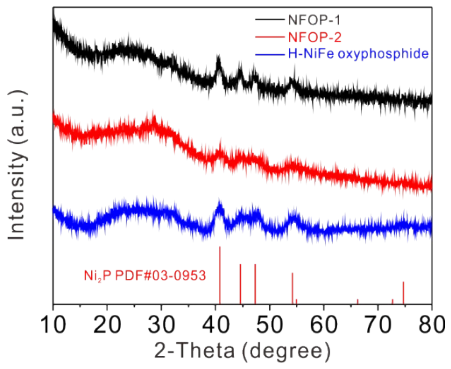

Fig. S23 XRD patterns of NFOP-1, NFOP-2, and H-NiFe oxyphosphide spheres. The XRD patterns show that NFOP-1 and NFOP-2 have similar diffraction peaks to those of H-NiFe oxyphosphide spheres.

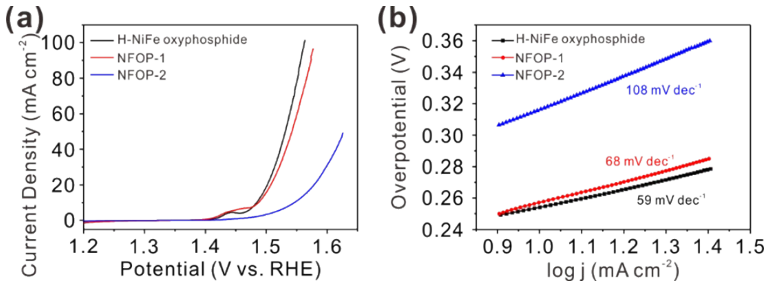

Fig. S24 (a) LSV curves and (b) Tafel plots of H-NiFe oxyphosphide, NFOP-1, and NFOP-2.

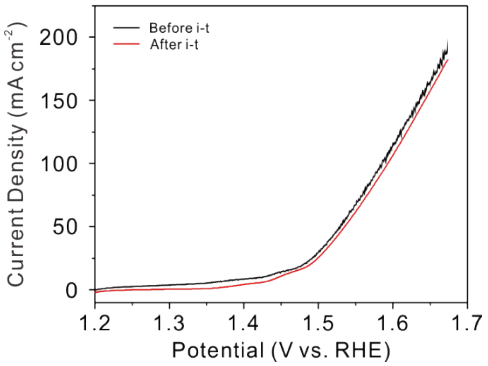

Fig. S25 LSV curves of H-NiFe oxyphosphide spheres before and after stability test.

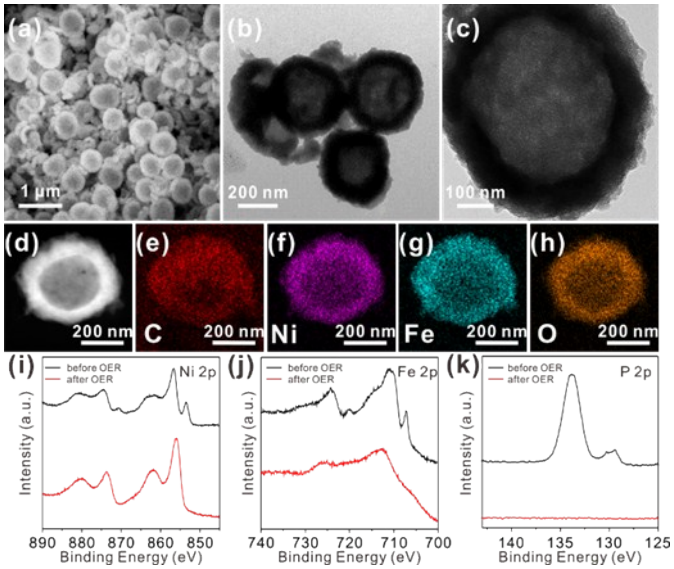

Fig. S26 (a) FESEM image, (b,c) TEM images, (d-h) HAADF-STEM image and corresponding elemental mapping images of H-NiFe oxyphosphide spheres after 20 hours of stability test. (i-k) XPS spectra of (i) Ni 2p, (j) Fe 2p, and (k) P 2p from H-NiFe oxyphosphide spheres before and after OER stability test.

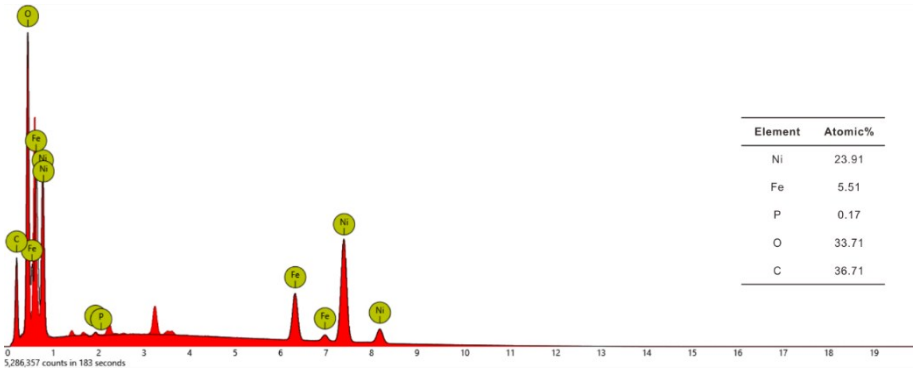

Fig. S27 EDX spectrum of H-NiFe oxyphosphide spheres after stability test.

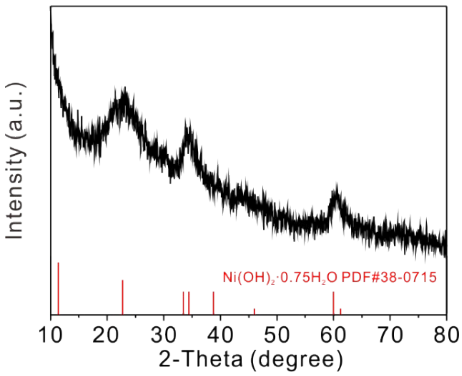

Fig. S28 XRD pattern of H-NiFe oxyphosphide spheres after stability test.

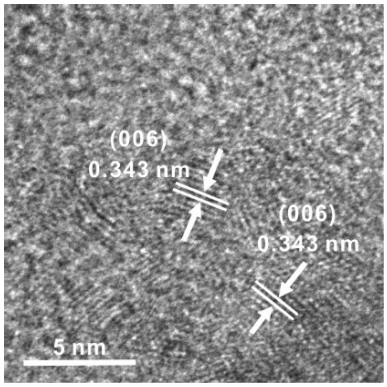

Fig. S29 HRTEM image of H-NiFe oxyphosphide spheres after stability test.

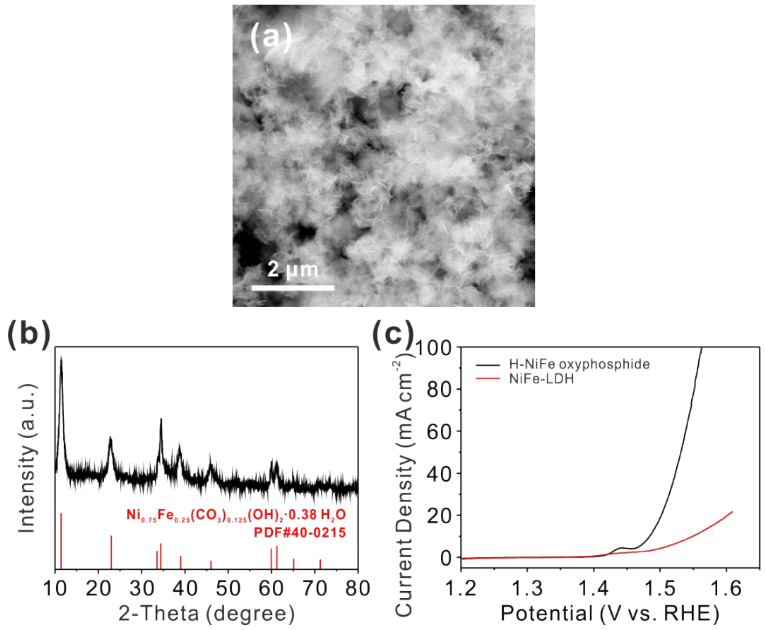

Fig. S30 (a) FESEM image of NiFe-LDH, (b) XRD pattern of NiFe-LDH, and (c) LSV curves of H-NiFe oxyphosphide spheres and NiFe-LDH.

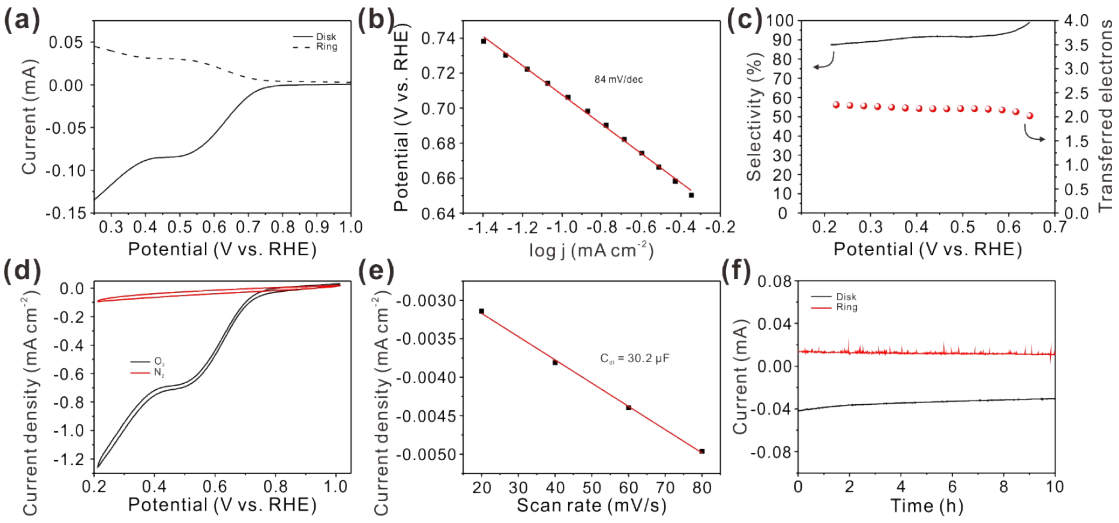

Fig. S31 (a) LSV curves of H-NiFe oxyphosphide spheres and the ring currents (dash line) measured at ring electrode in O_2-saturated 0.1 M KOH solution at a rotating speed of 1600 rpm, (b) Corresponding Tafel plots, (c) Calculated H_2O_2 selectivity and the electron transfer numbers of H-NiFe oxyphosphide spheres at different potentials measured by RRDE, (d) CV curves obtained in N_2-saturated 0.1 M KOH and O_2-saturated 0.1 M KOH, (e) Current density plotted as a function of different scan rates, (f) Long-term stability tests for H-NiFe oxyphosphide spheres measured by RRDE at a potential of 0.5 V *vs*. RHE.

Table S1. Comparison of the alkaline OER performance of hollow Ni-Fe oxyphosphide in this work with other recently reported metal phosphides-based pre-catalysts.

Catalysts	η@10 mA cm^{-2} (mV)	Tafel slope (mV dec^{-1})	Reference
Hollow NiFe oxyphosphide spheres	**253**	**59**	**This work**
Co-Fe oxyphosphide microtubes	280	53	[3]
Ni-Co-P hollow nanobricks	270	79	[4]
Carbon-incorporated nickel-cobalt mixed metal phosphide	330	96	[5]
CoMnP nanoparicles	330	61	[6]
FeP–rGO(70:30)@Au	280	49.6	[7]
$Ni_{0.6}Co_{1.4}P$ nanocages	300	80	[8]
Co_2P nanoneedles	310	50	[9]
Ni_2P nanoparticles	290	59	[10]
Multishelled Ni_2P sphere	270	40.4	[11]
Ni_2P/rGO	260	62	[12]
Ni-Fe phosphide nanoparticles encapsulated in N,P,S doped carbon	265	43	[13]
Fe, N-decorated Carbon-supported NiFeP nanoparticles	250	65	[14]
$Ni_{1.4}Fe_{0.6}P$@rGO	210	33	[15]

Supplementary references

1. J. H. Cheng, D. Zhao, L. S. Fan, X. Wu, M. X. Wang, N. Q. Zhang and K. N. Sun, *J. Mater. Chem. A*, 2017, **5**, 14519.
2. Q. Liu, L. S. Xie, Z. Liu, G. Du, A. M. Asiri and X. P. Sun, *Chem. Commun.*, 2017, **53**, 12446-12449.
3. P. Zhang, X. F. Lu, J. Nai, S. Q. Zang and X. W. Lou, *Adv. Sci.*, 2019, **6**, 1900576.
4. E. L. Hu, Y. F. Feng, J. W. Nai, D. Zhao, Y. Hu and X. W. Lou, *Energy Environ. Sci.*, 2018, **11**, 872.
5. P. He, X. Y. Yu and X. W. Lou, *Angew. Chem., Int. Ed.*, 2017, **56**, 3897.
6. D. Li, H. Baydoun, C. N. Verani and S. L. Brock, *J. Am. Chem. Soc.*, 2016, **138**, 4006.
7. J. Masud, S. Umapathi, N. Ashokaan and M. Nath, *J. Mater. Chem. A*, 2016, **4**, 9750.
8. B. C. Qiu, L. J. Cai, Y. Wang, Z. Y. Lin, Y. P. Zuo, M. Y. Wang and Y. Chai, *Adv. Funct. Mater.*, 2018, **28**.
9. A. Dutta, A. K. Samantara, S. K. Dutta, B. K. Jena and N. Pradhan, *ACS Energy Lett.*, 2016, **1**, 169.
10. L. A. Stern, L. G. Feng, F. Song and X. L. Hu, *Energy Environ. Sci.*, 2015, **8**, 2347.
11. H. M. Sun, X. B. Xu, Z. H. Yan, X. Chen, F. Y. Cheng, P. S. Weiss and J. Chen, *Chem. Mater.*, 2017, **29**, 8539.
12. L. T. Yan, H. M. Jiang, Y. L. Xing, Y. Wang, D. D. Liu, X. Gu, P. C. Dai, L. J. Li and X. B. Zhao, *J. Mater. Chem. A*, 2018, **6**, 1682.
13. P. Li and H. C. Zeng, *Chem. Commun.*, 2017, **53**, 6025-6028.
14. S. Ibraheem, S. G. Chen, J. Li, W. Li, X. Y. Gao, Q. M. Wang and Z. D. Wei, *ACS Appl. Mater. Interfaces*, 2019, **11**, 699-705.
15. M. Miao, R. Z. Hou, R. J. Qi, Y. Yan, L. Q. Gong, K. Qi, H. F. Liu and B. Y. Xia, *J. Mater. Chem. A*, 2019, **7**, 18925-18931.